ISSN 1070-3284, Russian Journal of Coordination Chemistry, 2019, Vol. 45, No. 4, pp. 253–265. © Pleiades Publishing, Ltd., 2019.
Russian Text © N.V. Cherkashina, A.V. Churakov, I.A. Yakushev, I.P. Stolyarov, V.N. Khrustalev, E.V. Khramov, A.A. Markov, N.S. Smirnova, Ya.V. Zubavichus, P.V. Dorovatovskii, Zh.V. Dobrokhotova, A.B. Ilyukhin, M.N. Vargaftik, 2019, published in Koordinatsionnaya Khimiya, 2019, Vol. 45, No. 4, pp. 197–210.

Dedicated to the 90th birthday of Academician I.I. Moiseev

The First Heterometallic Acetate-Bridged Pt(II)–Pd(II) Complex: Synthesis, Structure, and Formation of Bimetallic $PtPd_2$ Nanoparticles

N. V. Cherkashina[a], A. V. Churakov[a], I. A. Yakushev[a], I. P. Stolyarov[a], V. N. Khrustalev[b], E. V. Khramov[b, c], A. A. Markov[a], N. S. Smirnova[a], Ya. V. Zubavichus[c], P. V. Dorovatovskii[c], Zh. V. Dobrokhotova[a, †], A. B. Ilyukhin[a], and M. N. Vargaftik[a, *]

[a] *Kurnakov Institute of General and Inorganic Chemistry, Russian Academy of Sciences, Moscow, 119991 Russia*
[b] *Peoples' Friendship University of Russia, Moscow, 117198 Russia*
[c] *National Research Center Kurchatov Institute, Moscow, 123182 Russia*
**e-mail: wahr36@gmail.com*

Received September 11, 2018; revised October 3, 2018; accepted October 26, 2018

Abstract—The reaction of platinum acetate blue, empirically described as $Pt(OOCMe)_{2.50}$, with palladium(II) acetate $Pd_3(\mu\text{-}OOCMe)_6$ gave the first heterometallic acetate-bridged platinum(II) and palladium(II) complex $Pd_2Pt(\mu\text{-}OOCMe)_6$ (**I**) as co-crystallizates $17Pd_2Pt(\mu\text{-}OOCMe)_6 \cdot 4Pd_3(\mu\text{-}OOCMe)_6 \cdot 42C_6H_6$ (**IIa**) and $17Pd_2Pt(\mu\text{-}OOCMe)_6 \cdot 4\ Pd_3(\mu\text{-}OOCMe)_6$ (**IIb**). Single crystal X-ray diffraction (CIF files CCDC nos. 1568105 and 1852744), EXAFS, and quantum chemical studies (DFT and QTAIM) of complex **I** revealed a slightly distorted triangular structure similar to the structure of palladium(II) acetate $Pd_3(\mu\text{-}OOCMe)_6$ and hypothetical platinum(II) complex $Pt_3(\mu\text{-}OOCMe)_6$. The thermal decomposition of complex **IIa** gives the bimetallic alloy $PtPd_2$. A combined X-ray diffraction and EXAFS study demonstrated that the obtained material consists of core (Pt)–shell (Pd) particles with an average size of ~28 nm and a minor amount of smaller (~5 nm) PdO nanoparticles on the surface. The obtained results are useful for the understanding of the nature and structure of the supported phase of heterogeneous Pt–Pd catalysts.

Keywords: platinum, palladium, acetate complexes, synthesis, X-ray diffraction, crystal chemistry, quantum chemical analysis, nanoparticles

DOI: 10.1134/S107032841904002X

INTRODUCTION

The competition between platinum and palladium is significant for modern catalysis. In many cases, mixed-metal Pt–Pd catalysts have enhanced activity and selectivity in comparison with single-metal catalysts [1–5]. These catalysts are traditionally prepared by separate deposition of salts or complexes of desired metals (precursors) and subsequent redox treatment of the deposited material. In this study, we made an attempt to combine both metals in a heterometallic carboxylate complex, convert it to a heterometallic Pt–Pd nanomaterial via thermal decomposition, and to study the structure of the new material. The synthesis was carried out using the previously proposed process for the preparation of mixed-metal palladium(II) carboxylate complexes from the palladium acetate Pd3(μ-OOCMe)6 and di- and trivalent metal carboxylates [6–10]. Instead of using poorly accessible and low-reactive crystalline platinum(II) acetate Pt4(μ-OOCMe)8 as the initial platinum component, we used a noncrystalline material prepared in our previous study and characterized in detail, so-called platinum acetate blue (PAB) with the gross composition Pt(OOCMe)2.50 [11]. The reaction of PAB with Pd3(μ-OOCMe)6 in glacial acetic acid gave the crystalline complexes 17Pd2Pt(μ-OOCMe)6 · 4Pd3(μ-OOCMe)6 · 42C6H6 (IIa) and 17Pd2Pt(μ-OOCMe)6 · 4Pd3(μ-OOCMe)6 (IIb), which were studied by X-ray diffraction and EXAFS. The thermal decomposition of complex IIa was studied by DTA–TG, while the structure of platinum–palladium alloy nanoparticles formed upon thermolysis of IIa was investigated by DTA and EXAFS methods.

† Deceased.

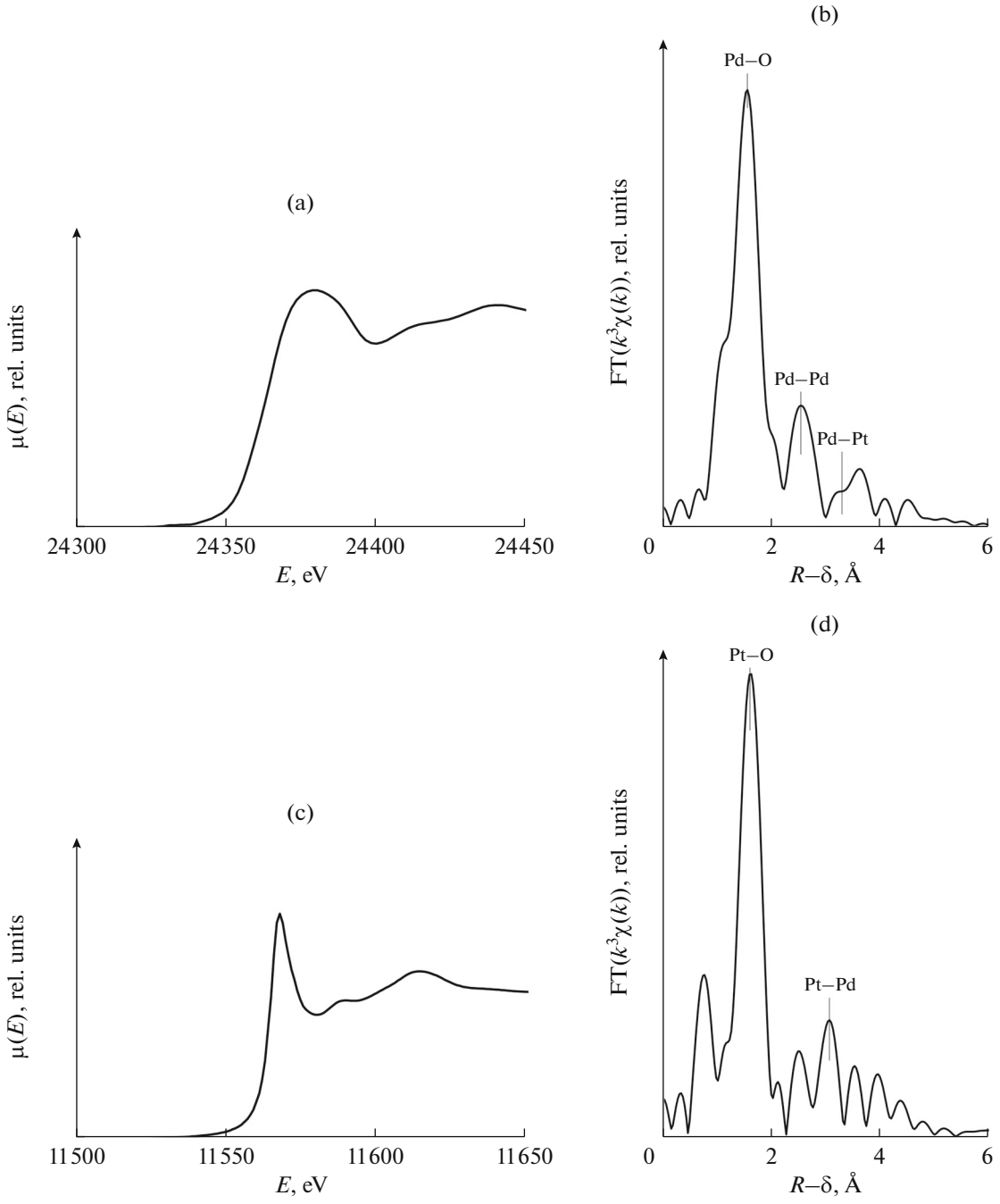

Fig. 1. XAFS data for polycrystalline **IIb** sample: (a, b) Pd*K*-edge and (c, d) PtL_3-edge.

RESULTS AND DISCUSSION

The heterometallic acetate-bridged platinum(II)–palladium(II) co-crystallizate **IIa** formed in the reaction of $Pd_3(\mu\text{-}OOCMe)_6$ with PAB in glacial acetic acid loses benzene molecules of crystallization to give complex **IIb**. The presence of both metals in the heterometallic part of complex **IIb** was proved by the XAFS method.

The palladium *K*-edge and platinum L_3-edge XAFS data for polycrystalline **IIb** unambiguously proved the presence of a platinum atom in the palladium coordination environment in the heterometallic part of the complex (Fig. 1, Table 1).

The palladium *K*-edge EXAFS spectrum was simulated by three coordination spheres. The most intense peak corresponds to four Pd–O distances (2.00 Å), while the next two peaks correspond

Table 1. Simulation parameters of the EXAFS spectra of polycrystalline sample **IIb***

Edge	Scattering atom	C.N.	R, Å	σ^2, Å^2	R_f, %
PdK	O	4.0**	2.00	0.0009	4.1
	Pd	1.0**	3.09	0.0030**	
	Pt	1.0**	3.42	0.0037***	
PtL_3	O	4.0**	1.97	0.0024	3.3
	Pd	2.0**	3.42	0.0037***	

* R is the interatomic distance; σ^2 is the Debye factor; R_f is the R-factor (relative error of fitting of experimental data).
** The parameters were fixed in the XAFS simulation.
*** The parameters were set equal in the combined simulation of Pd and Pt XAFS data.

to Pd–Pd and Pd–Pt coordination spheres. According to the simulation results, two palladium atoms are spaced by 3.09 Å. The low-intensity peak located at ~3.1 Å distance (on the R-δ scale) belongs to the Pd–Pt coordination sphere. The combined simulation of the Pt and Pd edge spectra showed the presence of the Pt atom at a 3.42 Å distance.

The PtL_3 edge Fourier transform EXAFS spectrum of molecule **IIb** was simulated by two coordination spheres. Like for the Pd K-edge, the first peak corresponds to four Pt–O distances at 1.97 Å, whereas the next, less intense peak is due to the Pt–Pd sphere with C.N. 2. The slight increase in the Pt–Pd distances compared with the model structure (3.31 Å) can be attributed to some disorder of the molecular structure or to the error of determination of the distance for more remote spheres.

Thus, PdK-edge and PtL_3-edge XAFS data unambiguously indicate that the Pt and Pd atoms are incorporated in the heterometallic core of molecule **IIb**. This conclusion was confirmed by X-ray diffraction, which provided more detailed structural information.

According to X-ray diffraction data (Figs 2, 3, Tables 2, 3), the crystals of **IIa** and **IIb** contain a heterometallic complex with the triangular metal core $Pd_2Pt(\mu\text{-}OOCMe)_6$, similar to the metal core of the known palladium(II)–copper(II) complex $Pd_2Cu(\mu\text{-}\mu OOCMe)_6 \cdot 2C_6H_6$ [6] and a somewhat different palladium(II) acetate metal core $Pd_3(\mu\text{-}OOCMe)_6$ [12, 13]. The triangular groups $Pd_2Pt(\mu\text{-}OOCMe)_6$ in the crystals of **IIa** and **IIb** are perpendicular to the crystallographic mirror plane passing through M_2 positions (M = Pd, Pt) and are perpendicular to the positions of acetate carbon atoms C(31) and C(41). In crystal **IIa**, M1 and M2 sites are partially occupied by palladium and platinum atoms with interatomic distance differing by less than 0.05 Å and occupancy ratios of 0.742(3)/0.258(3) and 0.708(3)/0.292(3), respectively (in crystal **IIb**, the occupancy ratios of the M1 and M2 sites are 0.740(13)/0.260(13) and 0.722(14)/0.278(14)). All metal atoms have a somewhat distorted square coordination. The Pd and Pt positions are somewhat shifted from the plane through four oxygen atoms towards the center of the molecule (by 0.227(4)–0.242(2) Å).

It is of interest that the metal core geometry in crystals **IIa** and **IIb** is determined by palladium rather than platinum atoms, while platinum(II) acetate has a nearly square structure $Pt_4(\mu\text{-}OOCMe)_8$ [14]. Meanwhile, the triangular core geometry of **IIa** changes insignificantly upon removal of the benzene molecules of crystallization and formation of **IIb** (Tables 2, 3).

In the crystal of **IIa**, heterometallic molecules are arranged in layers coinciding with the mirror planes $y = 1/4$ and $y = 3/4$. Thus, the interplanar spacing is $b/2$ = 11.4876 Å. The space between these layers is filled by the benzene molecules of crystallization linked by only weak T-shaped CH···π contacts. This fact is apparently responsible for the instability of crystal solvate **IIa** on storage in air. In the crystal of **IIb**, the complex molecules are arranged layer-by-layer in the same way as in **IIa** (Fig. 2), although the layers of benzene molecules are absent in the former case. As expected, these data attest to similar cell sizes a and c for **IIa** and **IIb** (Table 1).

The triangular geometry of the metal core in **I** is untypical of platinum(II) carboxylate. The Pt–Pt distance in the platinum(II) acetate molecule $Pt_4(\mu\text{-}OOCMe)_8$ [14] and in some known acetate-bridged platinum(II) complexes with a triangular metal core is 2.5–2.6 Å [15–18]. In contrast, the Pt–Pd distance found in molecule **I** is 3.16–3.18 Å (Table 1), as if it was determined by palladium atoms (for comparison, 3.1–3.2 Å in $Pd_3(\mu\text{-}OOCMe)_6$ [12, 13]).

Therefore, we studied the electron density distributione topology for molecule **I** $Pd_2Pt(\mu\text{-}OOCMe)_6$, for the complex $Pd_3(\mu\text{-}OOCMe)_6$, and for the hypothetical platinum complex $Pt_3(\mu\text{-}OOCMe)_6$ using the QTAIM method [19]. The calculation showed that the molecular graphs of all three triangular structures are quite similar (Fig. 4, Table 4).

The electron density values $\rho_b \approx 0.1$ a.u. and the electron density Laplacian $\nabla^2\rho_b \approx 0.5$ a.u. at the critical points of the metal–oxygen bond are typical of

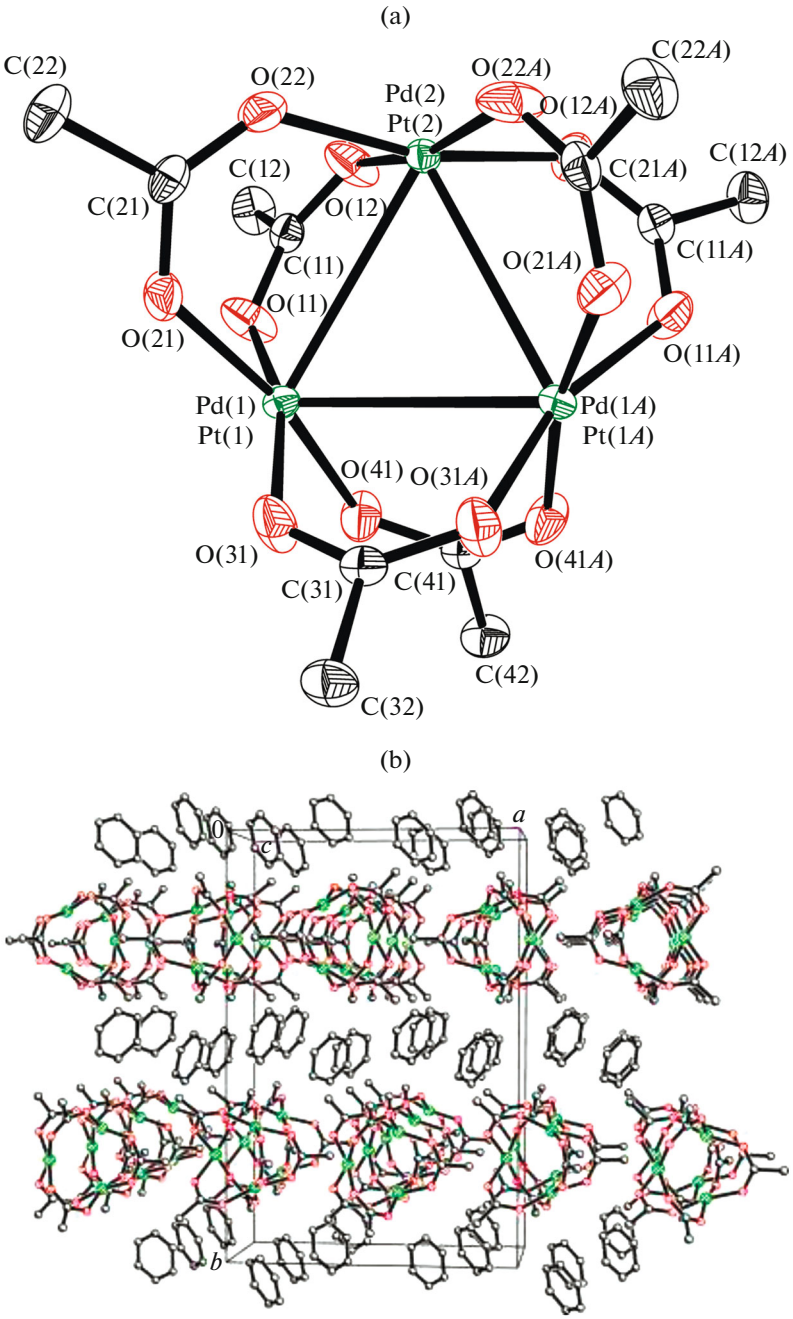

Fig. 2. (a) Molecular structure and (b) crystal packing of complex **IIa**, thermal ellipsoids are shown at 50% probability level. The hydrogen atoms are omitted.

interactions in closed-shell systems (ionic interactions), unlike the covalent interaction characterized by $\rho_b > 0.2$ a.u., while the $\nabla^2\rho b$ value is negative [20]. The delocalization index δ(M, O) (characterizing the bond order between the metal and oxygen atoms) is higher for the platinum–oxygen contact than for the palladium–oxygen contact, despite the almost identical interatomic distances. The metal–metal bond paths form a triangle with the cyclic critical point $\rho_b \approx 0.01$ a.u. The determined values $\rho_b \approx 0.02$ a.u. and $\nabla^2\rho_b \approx 0.05$ a.u. for the metal–metal bond critical points attest to weak interaction in the triangular metallacycle.

Thermal transformations of complex **IIa** under inert atmosphere (argon) include two stages (Fig. 5). The first (endothermic) step is associated with removal of benzene molecules of crystallization in the 50–90°C range. The second stage (sharp exotherm

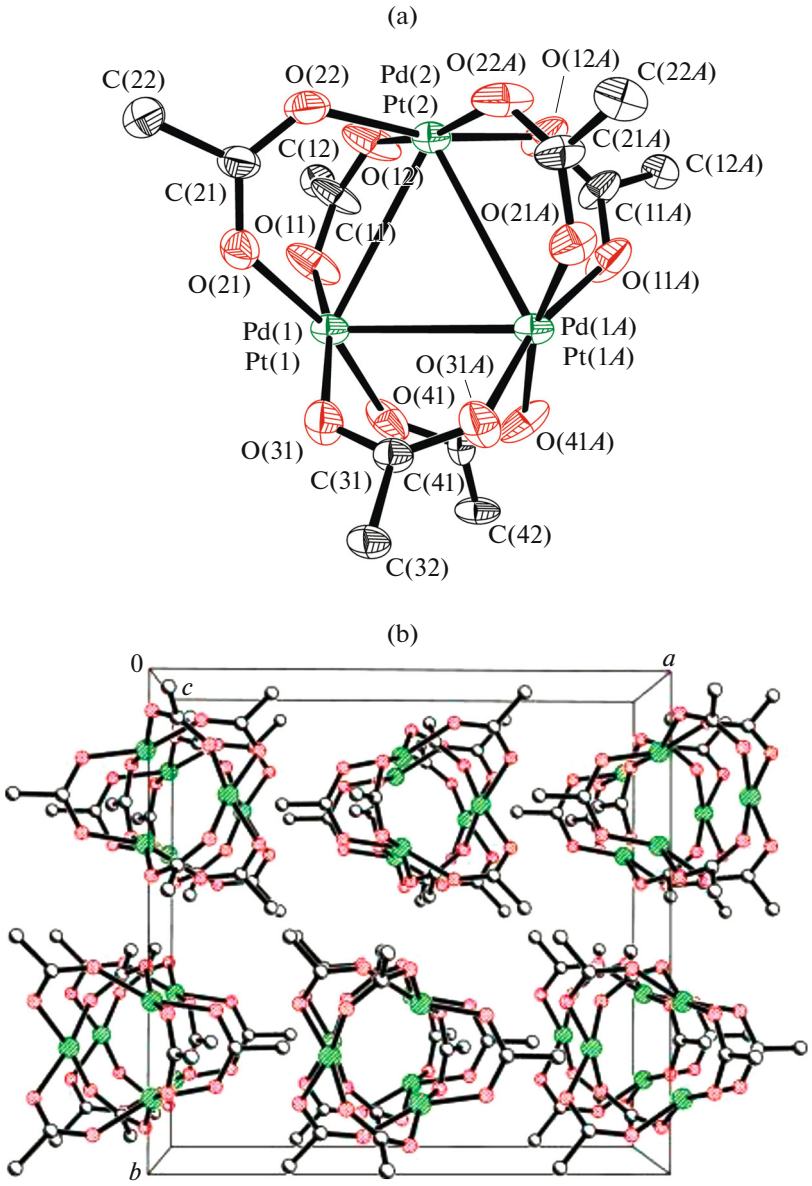

Fig. 3. (a) Molecular structure and (b) crystal packing of complex **IIb**, thermal ellipsoids are shown at 30% probability level. The hydrogen atoms are omitted.

followed by complex endotherm), associated with the removal of all acetate groups, is completed at ~220°C. The benzene molecules of crystallization are removed even during storage of the complex at room temperature; therefore, the first stage in the DTA–TG curves is diffuse and the mass loss observed at this stage (~7%) is much lower than the calculated value for the loss of two C_6H_6 molecules (~17%). Further heating does not induce any DTA–TG effects up to 400°C, so that the total mass loss (~50%) corresponds to complete decomposition of complex **IIa** to give bimetallic Pt–Pd alloy nanoparticles.

An X-ray diffraction study of the solid phase formed upon thermal decomposition of **IIa** showed the presence of two crystalline phases: Pd_xPt_{1-x} nanoalloy with the FCC lattice and ~28 nm particle size (coherent scattering region) and a minor amount (~7%) of smaller PdO particles with ~5 nm size (Fig. 6).

More detailed information on the structure of these Pd–Pt nanoparticles was gained by XANES/EXAFS studies (Figs. 7, 8).

The Pd*K*-edge XANES data (Fig. 7) show an oscillation contour typical of palladium metal. Nevertheless, the *K*-edge is somewhat shifted to higher energy, which implies either the presence of Pd–Pt bond or partial oxidation of palladium. Fitting of Pd*K*-edge

Table 2. Crystallographic data and structure refinement parameters of complexes **IIa** and **IIb**

Parameter	Value	
	IIa	**IIb**
Empirical formula	$C_{24}H_{30}O_{12}Pd_{2.19}Pt_{0.81}$	$C_{12}H_{18}O_{12}Pd_{2.20}Pt_{0.80}$
M	901.30	744.23
Color, habit	Orange prism	Orange prism
Crystal size, mm	0.20 × 0.15 × 0.15	0.05 × 0.03 × 0.03
Temperature, K	150	100
System	Orthorhombic	Orthorhombic
Space group	*Pnma*	*Pnma*
Unit cell dimensions:		
a, Å	15.5134(5)	15.533(3)
b, Å	22.9752(8)	15.007(3)
c, Å	8.2481(3)	8.3693(17)
V, Å^3	2939.82(18)	1950.9(7)
Z (*Z*')	4 (0.5)	4 (0.5)
ρ(calcd.), g/cm^3	2.036	2.534
μ, mm^{-1}	5.217	12.632
F(000)	1735	1424
θ_{min}–θ_{max}, deg	2.62–30.00	3.18–31.37
Ranges of reflection indices	$-21 \le h \le 21$, $-32 \le k \le 32$, $-11 \le l \le 11$	$-19 \le h \le 19$, $-19 \le k \le 18$, $-10 \le l \le 10$
Number of measured reflections	33832	28416
Number of unique reflections (R_{int})	4387 (0.0287)	2231 (0.0490)
Number of reflections with $I > 2\sigma(I)$	3933	1910
Reflections/restraints/parameters	4387/0/205	2231/24/152
R-factors for $I > 2\sigma(I)$	$R_1 = 0.0178$, w$R_2 = 0.0331$	$R_1 = 0.0495$, w$R_2 = 0.1281$
R-factors for all reflections	$R_1 = 0.0224$, w$R_2 = 0.0343$	$R_1 = 0.0574$, w$R_2 = 0.1356$
GOOF	1.067	1.043
Extinction coefficient		0.0051(5)
T_{max}/T_{min}	0.508/0.422	0.703/0.571
Residual electron density (min/max), e Å^{-3}	−0.625/0.456	−0.932/1.420

XANES data by a linear combination of data for Pd metal and the reference PdO spectrum made it possible to estimate the fraction of oxidized palladium as 7.1%. The major Fourier transform peak $k^3\chi(k)$ of the Pd*K*-edge spectrum has a somewhat higher intensity, which may attest to the presence of the Pd–Pt bond. The peak at $R \approx 2$ Å typical of the metal–oxygen distances attests to the possible presence of palladium oxide.

The PtL_3-edge XANES curve of the sample (Fig. 8) nearly coincides with the curve for Pt metal with a minor intensity difference. The Fourier transform $k^3\chi(k)$ of the PtL_3-edge spectrum has a lower intensity of the peak corresponding to the first coordination sphere and markedly shortened Pt–Pt distance, indicating the formation of an alloy.

The combined simulation of Pd and Pt edge XAFS data (the structural parameters found by simulation are summarized in Table 5) showed the following.

(1) The total C.N.(Pt) (according to the PtL_3-edge data), i.e., the total number $N_{Pd} + N_{Pt}$ of atoms located near a Pt atom at a ~2.7 Å distance is regularly overestimated and exceeds that for the Pt or Pd bulk metal ($N_b = 12$) or Pd_xPt_{1-x} solid solutions within the determination error (±1). Therefore, for structural correctness, in the final fitting of the $k^2\chi(k)$ value, the total C.N.(Pt) was taken to be 12. This assumption means that almost all platinum atoms are located inside the

Table 3. Selected distances (Å) and angles (deg) in molecules **IIa** and **IIb**

Distances and angles	**IIa**	**IIb**
Pd(1)···Pt(1)*	0.016(4)	0.291(13)
Pd(2)···Pt(2)	0.045(9)	0.275(11)
M(1)–M(1*A*)**	3.163(3)–3.173(3)	3.140(13)–3.36(2)
M(1)–M(2)	3.161(3)–3.183(4)	3.108(13)–3.322(14)
M(1)–O	1.982(3)–2.001(3)	1.929(10)–2.12(1)
M(2)–O	1.977(4)–2.017(4)	1.951(13)–2.019(14)
M(1)M(2)M(1*A*)***	59.80(6)–60.02(6)	59.6(3)–60.6(3)
M(2)M(1)M(1*A*)	59.82(6)–60.27(6)	57.3(2)–59.6(2)
cis-OM(1)O	85.5(1)–92.3(1)	86.1(5)–94.3(5)
trans-OM(1)O	163.7(1)–168.9(1)	163.7(6)–165.8(7)
cis-OM(2)O	83.5(2)–93.1(1)	83.8(8)– 91.8(4)
trans-OM(2)O	166.2(2)–167.0(2)	161.5(5)–174.0(8)

* Distances between Pd and Pt atoms occupying identical positions.
** M stands for Pd and Pt atoms in the same position.
*** Symmetry codes (*A*): x, $1.5 - y$, z.

Table 4. Results of DFT and QTAIM calculations for the acetate-bridged complexes $Pd_3(OOCMe)_6$, $Pd_2Pt(OOCMe)_6$ (**I**), and $Pt_3(OOCMe)_6$. The average values are given with standard deviations (in parentheses)

Parameters	$Pd_3(\mu\text{-}OOCMe)_6$	$Pd_2Pt(\mu\text{-}OOCMe)_6$ (**I**)	$Pt_3(\mu\text{-}OOCMe)_6$
M–M–M in the triangles			
R_1(M–M), Å	3.241(25)	Pd–Pd 3.177	3.144
R_2(M–M), Å		Pd–Pt 3.143, 3.249	3.230(9)
q(M)	0.965(1)	Pd 0.967, Pt 0.932	0.948(4)
ρ_b, a.u.	0.017(1)	Pd–Pd 0.018; Pd–Pt 0.023, 0.020	0.025(2)
$\nabla^2\rho_b$, a.u.	0.039(2)	Pd–Pd 0.044; Pd–Pt 0.052, 0.042	0.049(5)
ε_b*	0.096(9)	Pd–Pd 0.112; Pd–Pt 0.072, 0.117	0.038, 0.069(5)
δ(M,M)**	0.128(7)	Pd–Pd 0.132; Pd–Pt 0.197, 0.158	0.237, 0.198(5)
Oxygen atoms of the acetate bridging groups			
R(M–O), Å	2.007(5)	2.012(7)	2.014(5)
q(O)	−1.132(7)	−1.129(7)	−1.125(4)
ρ_b, a.u.	0.099(2)	0.102(6)	0.108(2)
$\nabla^2\rho_b$, a.u.	0.534(5)	0.534(13)	0.548(7)
ε_b*	0.164(10)	Pd 0.167(15), Pt 0.183(15)	0.190(14)
δ(M,O)**	0.632(10)	Pd 0.625(13), Pt 0.718(6)	0.709(7)

* Bond ellipticity characterizing the diffusiveness of electron density distribution in the plane perpendicular to the bond line.
** Delocalization index characterizing the bond order.

nanoparticle. Otherwise, that is, if a considerable part of Pt atoms were located on the surface or in a different phase with a different type of coordination, the coordination number $N_{Pd} + N_{Pt}$ would be systematically underestimated, as is the case for the Pd*K*-edge. The total C.N. ($N_{Pt} + N_{Pd}$) at the palladium edge is 10, which is considerably lower than that for the bulk metal. This can be interpreted in terms of a core–shell structure in which the platinum atoms tend to occur inside and the palladium atoms tend to reside on the

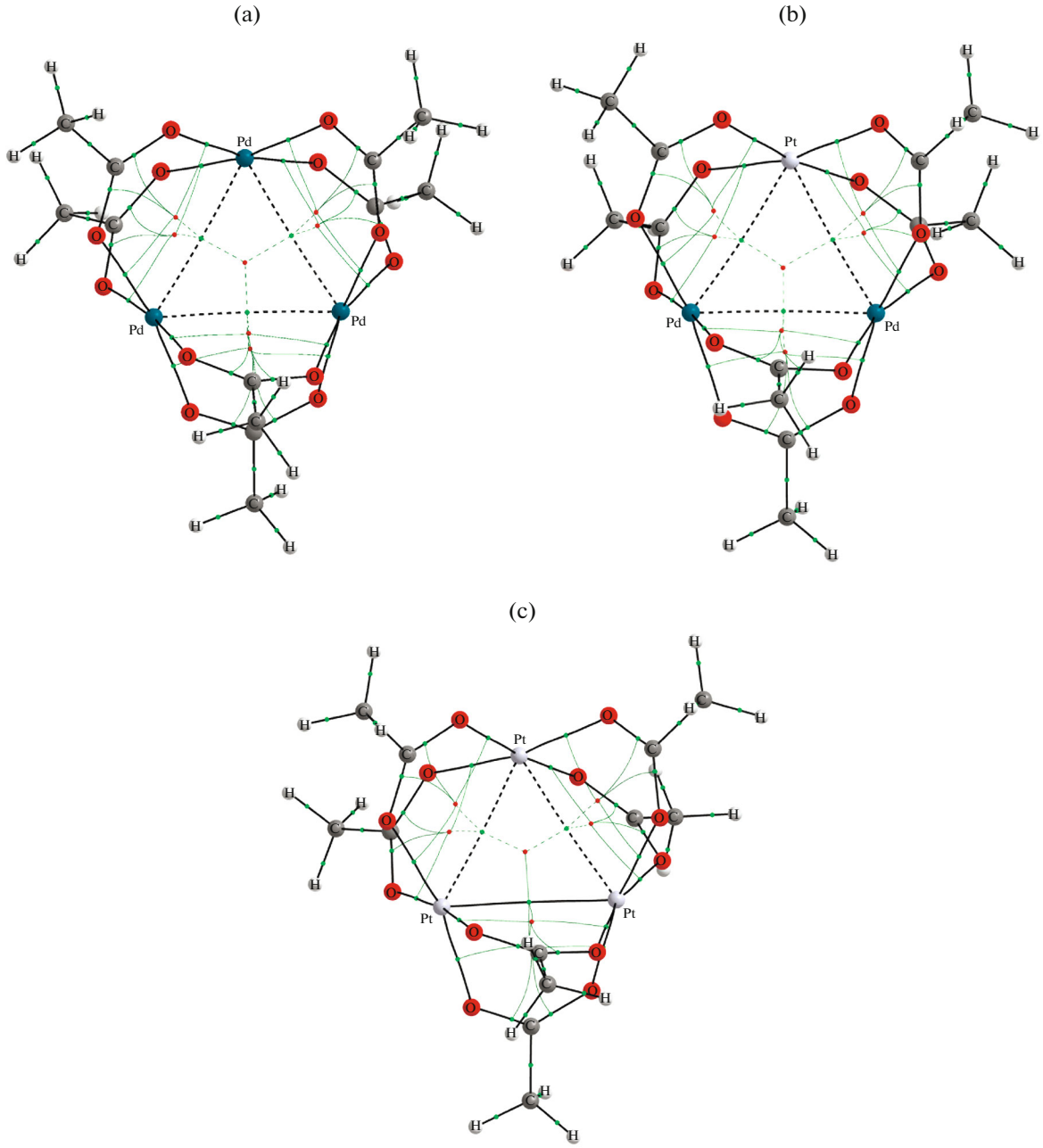

Fig. 4. Molecular graphs for (a) $Pd_3(OOCMe)_6$, (b) $Pd_2Pt(OOCMe)_6$, and (c) $Pt_3(OOCMe)_6$. The nuclear, bond, and cyclic critical points are shown. In the $Pt_3(OOCMe)_6$ structure, one Pt–Pt bond path is depicted as a continuous line (the ρ_b = 0.027 a.u. is somewhat higher than the threshold value 0.025 a.u.).

particle surface. Another possible explanation to the underestimated total C.N. for palladium is oxidation of some palladium atoms (PdO).

(2) The Pt–Pt and Pt–Pd coordination numbers do not differ significantly. The Pd–Pt C.N. is several-fold lower than the Pd–Pd C.N. The segregation parameters [21] calculated from the C.N. are J_{Pt} = 82% and J_{Pd} = 46%, respectively. This means that despite the decrease in the C.N. caused by partial oxidation of Pd atoms, the system tends to form core–shell structure. However, the platinum-enriched core also contains some quantity of palladium atoms, and the Pd and Pt atoms are distributed more or less homogeneously inside the particle core, whereas the shell consists mainly of Pd atoms, some of them being partially oxidized. The fraction of oxidized Pd atoms estimated from coordination numbers is ~7.0%, which is consistent with XANES data.

(3) The Pd–Pt, Pt–Pd, and Pd–Pd distances virtually coincide with the Pd–Pd distance in the first

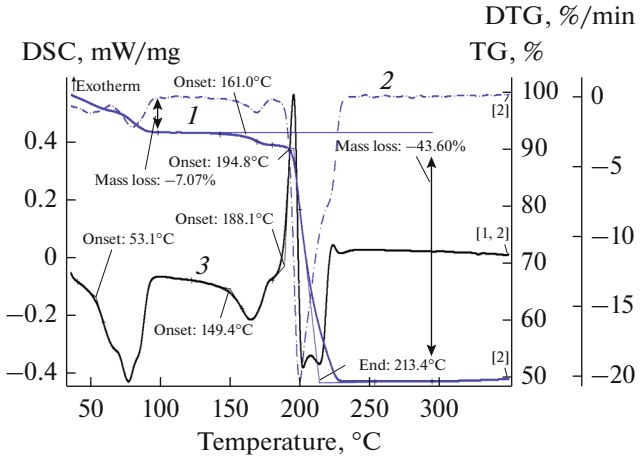

Fig. 5. DTA–TG data for **IIa** in an Ar flow at a heating rate of 10 deg/min: (*1*) TG, (*2*) DTG, (*3*) DSC.

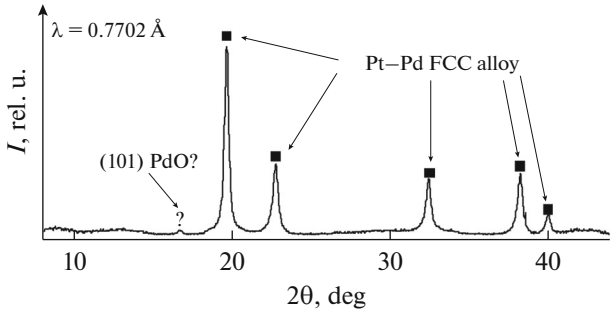

Fig. 6. X-ray diffraction pattern of a sample of bimetallic Pt–Pd nanoparticles.

coordination sphere of bulk palladium. However, the Pt–Pt distance is considerably shorter than not only the Pt–Pt distance in bulk platinum, but also the Pd–Pd distance in bulk palladium.

(4) High Debye factor for Pt–Pt (0.0072 Å^2) attests to considerable disorder of the platinum-enriched nanoparticle core.

Thus, the results obtained in this study confirmed the applicability of platinum acetate blue ($Pt(OOCMe)_{2.5}$, PAB) as the starting reactant for the synthesis of new platinum carboxylate complexes. Previously, using PAB, we synthesized trinuclear platinum(IV) complex with cobalt(II) $Pt^{IV}Co^{II}_2(\mu,\eta^2\text{-}OOCCMe_3)_4(OOCCMe_3)_2(OH)_2(HOOCCMe_3)_4$ [22], binuclear platinum(III) complexes $Pt^{III}_2(\mu\text{-}OOCMe)_4(O_3SMe)_2$ and $Pt^{III}_2(\mu\text{-}OOCMe)_4(O_3SPhMe)_2$ [23], and also binuclear platinum(II) complex $Pt^{II}(\mu\text{-}OOCMe)_4Co^{II}(OH_2)$ [11]. In this study, we employed this approach to prepare platinum(II) and palladium(II) complex **I** with a triangular metal core. The X-ray diffraction, EXAFS, and DFT–QTAIM quantum chemical data demonstrated that the structure of complex **I** with a somewhat distorted triangular metal core is similar to the structure of palladium acetate $Pd_3(\mu\text{-}OOCMe)_6$ and the hypothetical complex $Pt_3(\mu\text{-}OOCMe)_6$.

The thermal decomposition of complex **IIa** above 200°C under inert atmosphere gave a solid alloy with the composition $PtPd_2$. According to powder X-ray diffraction and XANES data, the obtained $PtPd_2$ alloy consisted of two nanosized crystalline phases, the Pd_xPt_{1-x} solid solution as the major component and the oxidized palladium PdO as the minor component. According to these results, the relatively large Pd_xPt_{1-x} nanoparticles with ~28 nm average size (CSR) consist of the platinum-enriched inner core and mainly palladium atoms in the outer region (Fig. 9).

The small quantity of partially oxidized palladium (PdO, ~5 nm average size) is apparently located on the surface of Pd_xPt_{1-x} nanoparticles. The lattice parameter (3.9032 Å) and the shortest Pd–Pd and Pd–Pt distances (2.74 Å) are close to the values for bulk palladium. Thus, the solid solution is based on a palladium matrix in which some Pd atoms have been replaced by Pt.

Table 5. Local structural parameters of the coordination environment of the Pt and Pd atoms from the best fitting results of the EXAFS Fourier transform for Pd–Pt alloy nanoparticles and two standards (bulk Pd and Pt metals)*

Sample	Edge	Scattering atom	C.N.	*R*, Å	σ^2, Å^2	R_f, %
Pt–Pd nanoalloy	PtL_3	Pt	5.6	2.71	0.0072	0.5
		Pd	6.4	2.74	0.0051	
	Pd*K*	Pd	7.8	2.74	0.0049	0.6
		Pt	1.5	2.74	0.0012	
		O	0.7	2.00	0.0080	
Pd foil	Pd*K*	Pd	12.0	2.74	0.0047	1.0
Pt foil	PtL_3	Pt	12.0	2.77	0.0048	0.1

* *R* is the interatomic distance; σ^2 is the Debye–Waller factor, R_f is the fitting factor.

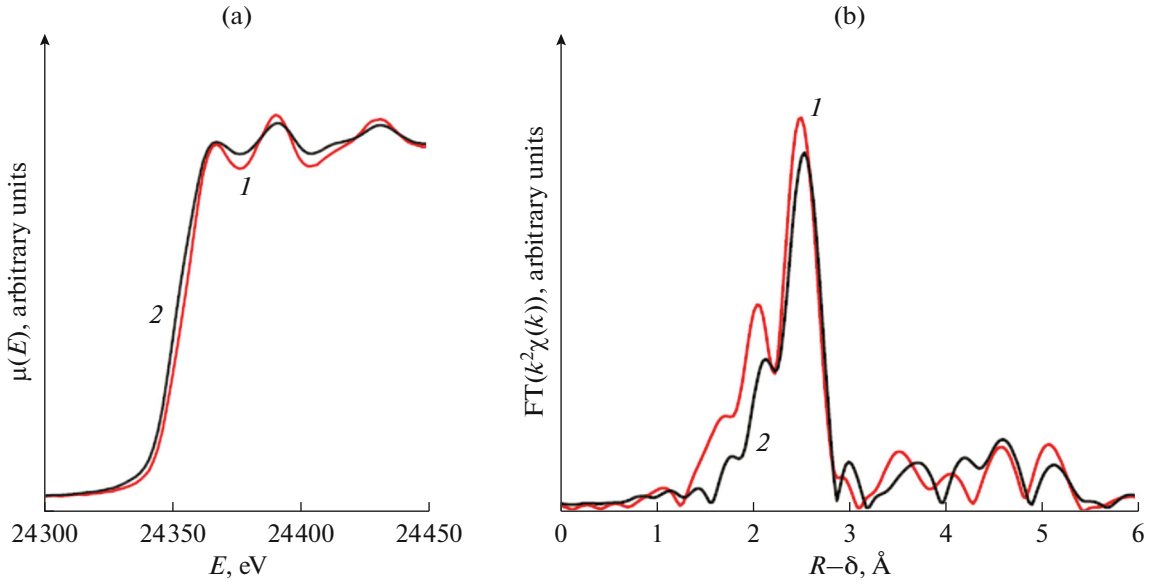

Fig. 7. Pd*K*-edge (a) XANES and (b) EXAFS data for (*1*) Pd–Pt nanoparticles and (*2*) Pd foil standard.

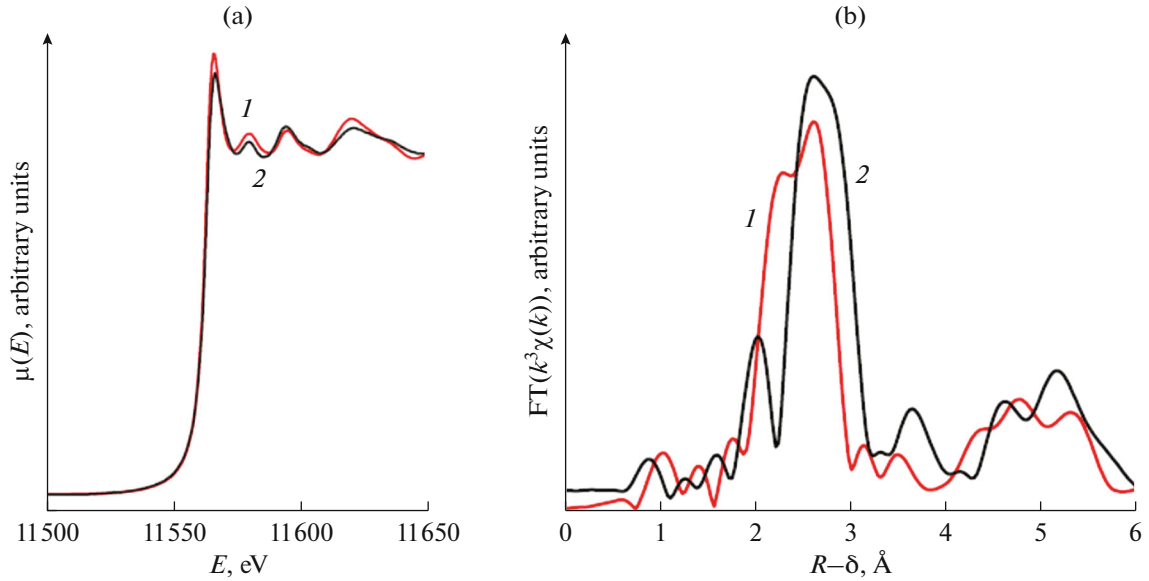

Fig. 8. PtL_3-edge (a) XANES and (b) EXAFS data for (*1*) Pd–Pt nanoparticles and (*2*) Pt black standard.

The obtained results are consistent with the data of previously published experimental (in particular, EXAFS) [24] and theoretical [25] studies on bimetallic Pt–Pd nanoparticles with different Pt to Pd ratios. According to previous conclusions [24, 25], the Pt–Pd core–shell nanoparticles are energetically more favorable than structures with homogeneous distribution of the metals. For relatively small (2–3 nm) nanoparticles, it was shown previously that platinum tends to be located in the inner part of nanoparticles, with palladium atoms being displaced to the periphery [24, 25]. According to results of our study, this conclusion holds for large nanoparticles of ~28 nm size.

The results we obtained shed some light on the nature of the supported phase of bimetallic Pt–Pd catalysts.

EXPERIMENTAL

The solvents used in this study (glacial acetic acid and benzene (reagent grade, Reakhim, Russia) were

purified by standard procedures [26]. Palladium(II) acetate $Pd_3(OOCMe)_6$ (reagent grade, Reakhim, Russia) was purified by refluxing in glacial acetic acid with freshly prepared palladium black and recrystallization from acetic acid. The PAB $Pt(OOCMe)_{2.50}$ was prepared from H_2PtCl_6 (reagent grade, Reakhim, Russia) by a reported procedure [11].

Elemental C,H,N-analysis was performed on a EuroVector EA3000 automated C,H,N-analyzer (Italy, 2008). FT IR spectra were measured on a Nicolet Nexus 460 spectrometer. The optical spectra were recorded on a Varian Cary 50 spectrophotometer.

Synthesis of $17Pd_2Pt(\mu\text{-}OOCMe)_6 \cdot 4Pd_3(\mu\text{-}OOCMe)_6 \cdot 42C_6H_6$ (IIa). Platinum acetate blue (PAB) $Pt(OOCMe)_{2.5}$ (190.6 mg, 0.556 mmol) and palladium acetate $Pd_3(OOCMe)_6$ (124.5 mg, 0.556 mmol) in glacial acetic acid (100 mL) were magnetically stirred at 80°C for 19 h until a dark brown solution formed. The solution was filtered and evaporated to dryness on a rotary evaporator. The dry residue was extracted several times with 20-mL portions of benzene until the solution was colorless. The combined benzene extracts were slowly evaporated in air. The yield of the dark orange crystals $17Pd_2Pt(OOCMe)_6 \cdot 4Pd_3(OOCMe)_6 \cdot 42C_6H_6$ was 70.3 mg (33% based on Pd).

For $C_{18}H_{21}O_{12}Pd_{2.19}Pt_{0.81}$

Anal. calcd., %	C, 26.35	H, 2.58	Pt + Pd, 47.67
Found, %	C, 26.11	H, 2.21	Pt + Pd, 48.46

IR (ATR; ν, cm^{-1}): 1600 vs, 1479 w, 1427 vs, 1350 m, 1042 w, 950 w, 696 m, 622 w, 552 w. UV-Vis (AcOH; ν, nm): 609, 400, 305.

Synthesis of $17Pd_2Pt(\mu\text{-}OOCMe)_6 \cdot 4Pd_3(\mu\text{-}OOCMe)_6$ (IIb). Complex **IIa** readily loses benzene molecules of crystallization on storage in air. After 3 days and after drying in a vacuum dessicator above wax, no benzene was found in the product. According to microanalysis data, the content of organic matter has decreased in accordance with the composition $17Pd_2Pt(OOCMe)_6 \cdot 4Pd_3(OOCMe)_6$.

For $C_{12}H_{15}O_{12}Pd_{2.20}Pt_{0.80}$

Anal. calcd., %	C, 19.06	H, 2.08
Found, %	C, 19.21	H, 2.13

X-ray diffraction data confirmed the retention of the acetate-bridged Pd_2Pt structure of **IIb** after removal of benzene molecules from **IIa**.

X-ray diffraction data for **IIa** were collected on a Bruker SMART APEX II diffractometer in the ω-scan mode at the Center for Collective Use of the Kurnakov Institute of General and Inorganic Chemistry, Russian Academy of Sciences. The X-ray diffraction data for complex **IIb** were obtained using the Protein X-ray beam at the Kurchatov Synchrotron Radiation Center of the National Research Center, Kurchatov Institute (Moscow, Russian Federation) in the φ-scan mode with a Rayonix SX165 CCD detector at 150 and 100 K. The primary indexing, refinement of parameters, and integration of reflections were performed using the iMOSFLM program of the CCP4 package [27] and the Bruker SAINT software [28]. The absorption corrections to the reflection intensity were applied using the Scala [29] and SADABS [30] programs. The structures were solved by direct methods and refined by the full-matrix least-squares method on F^2 with anisotropic approximation for all nonhydrogen atoms. The hydrogen atoms were placed into calculated positions and refined in the riding model with $U_{iso}(H) = 1.5U_{eq}(C)$ for methyl groups and $1.2U_{eq}(C)$ for benzene molecules of crystallization. For the crystal of **IIa**, the Pd and Pt partial coordinates, thermal parameters, and occupancies were refined independently without restraints. In the case of **IIb**, EADP instructions were used for positions of both metals due to insufficient crystallinity of the sample.

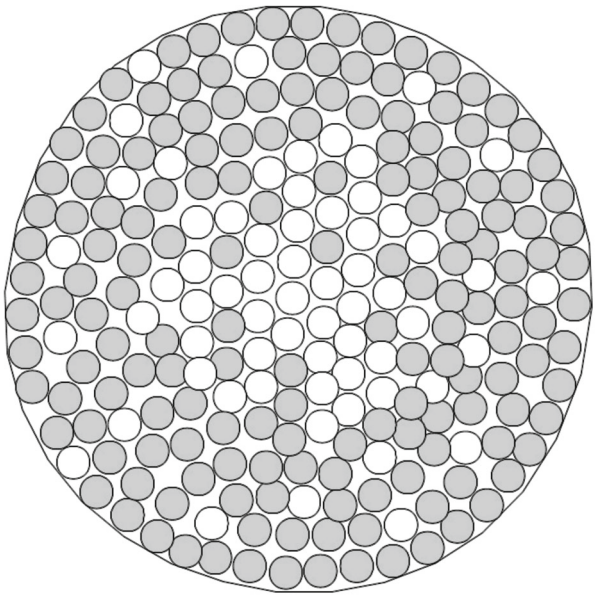

Fig. 9. Schematic structure of a nanosized Pd–Pt alloy particle: Pd is a gray circle, Pt is a white circle.

The calculations were carried out using the SHELXTL program package [30]. Crystallographic data for complexes **IIa** and **IIb** are deposited with the Cambridge Crystallographic Data Centre (CCDC no. 1568105 and no. 1852744, respectively).

The thermal decomposition of complex **IIa** was studied by calorimetry (DSC) and thermogravimetry (TG) in an argon flow (20 mL/min) in the 20–400°C range. The TG curves were recorded on a TG 209 F1 instrument in alundum crucibles at a heating rate of

10°C/min. DSC data were gained on a DSC 204 F1 instrument in aluminum crucibles at a heating rate of 10°C/min. Each experiment was performed at least in triplicate. The results of measurements were processed in accordance with ISO 11357-1, ISO 11357-2, ISO 11358, and ASTM E 1269-95 using the NETZSCH Proteus Thermal Analysis program package.

XANES and EXAFS. Pd*K*- and PtL_3-edge EXAFS spectra were measured in the transmission mode. The X-ray beam intensity before and after passage through the sample was measured in air-filled and Ar-filled ionization chambers. After the second chamber, one more Ar-filled ionization chamber was located for measuring the reference spectra of Pt and Pd metals for calibration. The energy scanning was performed using a Si (220) single crystal monochromator with energy resolution $\Delta E/E \approx 2 \times 10^{-4}$. The primary processing of the XAFS spectra employed the IFEFFIT program package [31, 32]. The normalized EXAFS k^3-oscillations were analyzed in the 2.0–12.5 Å^{-1} range for Pd*K*- and PtL_3-edges. The Fourier transforms of the EXAFS oscillations were fitted in the 1–3 Å range.

Quantum chemical calculations. The equilibrium geometry of the molecules was calculated by the DFT method with the PBE0 GGA hybrid functional [33] in the spin-restricted version using the GAMESS-US program package [34]. The relativistic effects for the palladium and platinum atoms were included by applying the third order Douglas–Kroll correction and the Sapporo-DK-DZP basis set [35–38]. QTAIM calculations were carried out using the AIMAll program package [39].

ACKNOWLEDGMENTS

X-ray spectroscopy studies (XANES and EXAFS) and quantum chemical calculations were supported by the Russian Science Foundation (project no. 18-73-10206). The work was supported by the Russian Foundation for Basic Research (projects nos. 17-03-00355, 18-03-00228, 18-33-00632) and the Program "5-100" of the Russian People's Friendship University. Equipment of the Center for Collective Use of Physical Investigation Methods, Kurnakov Institute of General and Inorganic Chemistry, Russian Academy of Sciences, was used.

XRD studies of of the complex **IIb** were carried out with the support of the National Research Center Kurchatov Institute (Order 2683 of November 25, 2018).

REFERENCES

1. Chen, M. and Schmidt, L.D., *J. Catal.*, 1979, vol. 56, p. 198.
2. Lee, Y.W., Ko, Y.A.R., Kim, D.Y., et al., *RSC Adv.*, 2012, vol. 2, p. 1119.
3. Morlang, A., Neuhausen, U., Klementiev, K.V., et al., *Appl. Catal., B*, 2005, vol. 60, p. 191.
4. Lapisardi, G., Gélin, P., Kaddouri, A., et al., *Top. Catal.*, 2007, vols 42–43, p. 461.
5. Wang, W., Wang, Z., Wang, J., et al., *Adv. Sci.*, 2017, p. 1600486.
6. Kozitsyna, N.Yu., Nefedov, S.E., Dolgushin, F.M., et al., *Inorg. Chim. Acta*, 2006, vol. 359, p. 2072.
7. Tkachenko, O.P., Stakheev, A.Yu., Kustov, L.V., et al., *Catal. Lett.*, 2006, vol. 112, p. 155.
8. Kozitsyna, N.Yu., Nefedov, S.E., Dobrokhotova, Zh.V., et al., *Nanotechnol. Russ.*, 2008, vol. 3, p. 100.
9. Nefedov, S.E., Kozitsyna, N.Yu., Vargaftik, M.N., et al., *Polyhedron*, 2009, vol. 28, p. 172.
10. Nefedov, S.E., Kozitsyna, N.Yu., Akhmadullina, N.S., et al., *Inorg. Chem. Commun.*, 2011, vol. 14, p. 554.
11. Cherkashina, N.V., Kochubey, D.I., Kanazhevskiy, V.V., et al., *Inorg. Chem.*, 2014, vol. 53, p. 8397.
12. Skapski, A.C. and Smart, M.L., *J. Chem. Soc., Chem. Commun.*, 1970, p. 658.
13. Cotton, F.A. and Han, S., *Revue de Chimie Minerale*, 1985, vol. 22, p. 277.
14. Carrondo, M.A.A.F. and Skapski, A.C., *Acta Crystallogr., Sect. B: Struct. Crystallogr. Cryst. Chem.*, 1978, vol. 34, p. 3576.
15. Yamaguchi, T., Nishimura, N., and Ito, T., *J. Am. Chem. Soc.*, 1993, vol. 115, p. 1612.
16. Yamaguchi, T., Nishimura, N., Shirakura, K., et al., *Bull. Chem. Soc. Jpn.*, 2000, vol. 73, p. 775.
17. Yamaguchi, T. and Ito, T., *Adv. Inorg. Chem.*, 2001, vol. 52, p. 205.
18. Murahashi, T., Usui, K., Inoue, R., et al., *Chem. Sci.*, 2011, vol. 2, p. 117.
19. Bader, R., *Atoms in Molecules: A Quantum Theory*, Oxford (USA): Oxford Univ., 1994.
20. *The Quantum Theory of Atoms in Molecules: From Solid State to DNA and Drug Design*, Matta C.F. and Boyd R.J., Eds., Weinheim: Wiley, 2007.
21. Hwang, B.-J., Sarma, L.S., Chen, J.-M., et al., *J. Am. Chem. Soc.*, 2005, vol. 127, p. 11140.
22. Nefedov, S.E., Kozitsyna, N.Yu., Cherkashina, N.V., et al., *Inorg. Chem. Commun.*, 2006, vol. 9, p. 1026.
23. Cherkashina, N.V., Nefedov, S.E., Klyagina, A.P., et al., *Inorg. Chem. Commun.*, 2012, vol. 21, p. 39.
24. Rades, T., Pak, C., Polisset-Thfoin, M., et al., *Catal. Lett.*, 1994, vol. 29, p. 91.
25. Huang, R., Wen, Y.H., Zhu, Z.Z., et al., *J. Phys. Chem. C*, 2012, vol. 116, p. 8664.
26. Perrin, D.D. and Armarego, W.L.F., *Purification of Laboratory Chemicals*, Oxford: Pergamon, 1988.
27. Battye, T.G.G., Kontogiannis, L., Johnson, O., et al., *Acta Crystallogr., Sect. D*: *Biol. Crystallogr.*, 2011, vol. 67, p. 271.
28. *SAINT Area-Detector Integration Sofware, 2012*, Madison: Bruker AXS Inc., 2012.

29. Evans, P.R., *Acta Crystallogr., Sect. D*: *Biol. Crystallogr.*, 2006, vol. 62, p. 72.
30. Evans P.R., *Acta Crystallogr., Sect. C: Struct. Chem.,* 2015, vol. 71, p. 3.
31. Ravel, B. and Newville, M., *Synchrotron Radiat.*, 2005, vol. 12, p. 537. doi 10.1107/S0909049505012719
32. Newville, M., *J. Synchrotron Radiat.*, 2001, vol. 8, p. 322. doi 10.1007/978-3-319-03762-2
33. Adamo, C. and Barone, V., *J. Chem. Phys.*, 1999, vol. 110, p. 6158.
34. Schmidt, M.W., Baldridge, K.K., Boatz, J.A., et al., *J. Comput. Chem.*, 1993, vol. 14, p. 1347.
35. Matsuoka, O., *Bull. Univ. Electron. Commun.*, 1992, vol. 5, p. 23.
36. Noro, T., Sekiya, M., and Koga, T., *Theor. Chem. Accounts*, 2003, vol. 109, p. 85.
37. Noro, T., Sekiya, M., and Koga, T., *Theor. Chem. Accounts*, 2012, vol. 131, p. 1124.
38. Noro, T., Sekiya, M., and Koga, T., *Theor. Chem. Accounts*, 2013, vol. 132, p. 1363.
39. Keith, T.A., *AIMAll (version 16.05.18)*, Overland Park: TK Gristmill Software, 2016.

Translated by Z. Svitanko